Quantitatively analyzing microscopic mechanism of phonon coupling in nanostructured diamond

Wu Liang[1], Shixian Liu[2], Han Meng[1*], Nuo Yang[1]

[1] College of Science, National University of Defense Technology, Changsha, 410073, China.

[2] Independent Researcher, Xinzhou 034000, China.

*Corresponding authors: menghan@nudt.edu.cn (H. M.)

Abstract

By combining nonequilibrium molecular dynamics, the spectral phonon temperature method, and the phonon weak-coupling model, we quantify the coupling between longitudinal and transverse phonon mode groups in nanostructured diamond. At 300 K and a system length of approximately 35 nm, the selected LP and TP modes along Γ-X retain a resolvable temperature difference, yielding a coupling length of 130 ± 34 nm and indicating weak coupling. From 300 to 700 K, the coupling length decreases overall with increasing temperature, whereas above 700 K the temperature difference becomes too small for stable PWCM fitting. The coupling length increases with system length, which may mainly arise from the size dependence of thermal conductivity. These results demonstrate that distinct phonon mode groups in high-thermal-conductivity diamond can remain in local thermal nonequilibrium over nanoscale distances. These results characterize branch-resolved thermal nonequilibrium in nanostructured diamond.

1. Introduction

Phonon engineering has enabled major advances in chip thermal management, aerospace thermal protection, and thermoelectric conversion[1–5]. At the micro and nanoscale, Fourier's law breaks down, and phonon transport exhibits more complex mechanisms[6–11]. Central to these mechanisms is the coupling strength between phonon branches, which directly governs thermal conductivity, scattering phase space, and the emergence of local thermal nonequilibrium[12–16]. In low-dimensional nano systems, the interaction between phonons is typically characterized as weak coupling. This weak coupling physics has been shown to underpin numerous anomalous heat conduction phenomena at small scales, and preliminary progress has been made in characterizing mode-specific temperatures and inter-branch coupling in low-dimensional system[10,17–22]. However, existing studies have concentrated almost exclusively on two-dimensional materials, leaving a critical gap in the understanding of phonon coupling strength in three-dimensional crystals[23–28]. Cubic diamond, with a room-temperature thermal conductivity exceeding 2200 W/ (m · K) and widespread use in semiconductors, high-power electronics, aerospace, and quantum technologies, is a prime candidate for such investigation[29–33]. But the coupling between its longitudinal and transverse phonon modes has not been quantitatively characterized. In this work, we combine nonequilibrium molecular dynamics (NEMD), the spectral phonon temperature method (SPT) [28], and the phonon weak coupling model (PWCM) [34,35] to study coupling between longitudinal (LP) and transverse phonon (TP) mode groups in nanostructured diamond. Atomic velocities are projected onto phonon polarization eigenvectors along Γ-X to obtain the spatial temperatures of the LP and TP modes. Their resolvable temperature difference demonstrates local thermal nonequilibrium. At 300 K and a system length of approximately 35 nm, PWCM fitting gives a coupling length of 130 ± 34 nm. The LP/TP coupling strengthens with temperature, whereas the coupling length increases with

system size because of the size dependence of thermal conductivity. These findings establish a benchmark for inter-branch phonon coupling in nanostructured diamond and provide a physical basis for engineering diamond-based thermal solutions.

2. Model and method

The heat transport in nanostructured diamond was investigated using nonequilibrium molecular dynamics (NEMD). The simulation cell and the corresponding boundary regions are illustrated in Fig. 1. As shown in Fig. 1(a), diamond has a three-dimensional tetrahedrally bonded crystal structure. Figure 1(b) shows the NEMD configuration, including the fixed layers, the Langevin heat-source and heat-sink regions, the internal free-transport region, and the branch-selective velocity-constraint region. The x axis is parallel to the [100] crystallographic direction and defines the heat-flow direction. Fixed boundary conditions were applied along x, with the outermost atomic layers fixed to eliminate rigid-body translation, whereas periodic boundary conditions were applied along the transverse y and z directions.

All NEMD simulations were performed using the Large-scale Atomic/Molecular Massively Parallel Simulator (LAMMPS) [36]. The carbon-carbon interactions were described using the Tersoff empirical potential [39,40], which has been widely used to reproduce the structural and lattice-dynamical properties of diamond. The potential parameters and other simulation details are provided in the Supporting Information. The equations of motion were integrated using the velocity Verlet algorithm with a time step of 0.5 fs. The system was equilibrated for 100 ps in the NPT ensemble at 300 K. Langevin baths at 310 K and 290 K were then applied at the two ends to establish a steady heat flow along x, while atoms outside fixed and bath regions were integrated in NVE. After a 400 ps nonequilibrium pre-run, a 5 ns production run was performed. Velocities were recorded every 5 fs for SPT. Independent simulations used different initial-velocity random seeds. Full parameters are given in the Supporting Information.

Seven atomic layers are used for each Langevin bath [37,38]. The source and sink temperatures are 310 and 290 K, respectively. The seven-layer bath is approximately two conventional diamond cells thick along x, so energy is injected and removed over a finite region rather than at one atomic plane. To examine finite-size and fixed-boundary effects, SPT temperature profiles were compared for short-, intermediate-, and long-wave modes along Γ-X (Fig. S5). The long- and intermediate-wave modes show stronger boundary sensitivity and quasiballistic behavior, whereas the short-wave modes vary more continuously in the internal free-transport region. The latter are therefore used for LP/TP temperature-difference analysis and PWCM fitting. Fixed layers, baths, the selective-constraint region, and bins adjacent to both interfaces are excluded from the fit.

As shown in Fig. 1(b), A branch-selective velocity-constraint region is placed at one end of the system to establish a nonequilibrium boundary condition between the LP and TP modes, for atoms in the control region to the left of the dashed line, no additional constraints were applied. For atoms in the restricted region to the right of the dashed line, the x-component of the vibrational velocity was forced to zero, effectively freezing the longitudinal polarization. This treatment follows the use of selective boundaries in electron–phonon two-temperature models and previous PWCM studies. The constraint creates an LP/TP temperature difference near the interface but is not used to define the phonon eigenbranches. Although it perturbs the local vibrational state in and near the constrained region, this region is excluded from the subsequent SPT–PWCM analysis. The heat flow is along x || [100], and the analyzed wave vectors lie on Γ-X with $\boldsymbol{q}$ || [100]. Modes with polarization parallel to $\boldsymbol{q}$ are assigned to LP, whereas modes with polarization perpendicular to $\boldsymbol{q}$ are assigned to TP. Their spatial temperatures are obtained by projecting NEMD velocities onto the corresponding polarization eigenvectors. Fixed layers, thermal baths, the constrained region, and bins adjacent to the bath and constrained interfaces are

excluded from the PWCM fit.

To obtain spatial temperatures of longitudinal and transverse phonon eigenmodes, we use the spectral phonon temperature (SPT) [28] method to project NEMD velocity trajectories onto lattice-dynamical eigenmodes. Phonon frequencies and polarization eigenvectors are first obtained from lattice dynamics. For a mode specified by wave vector $\boldsymbol{q}$ and branch index λ, the mass-weighted normal-mode velocity is

$$\dot{Q}_\lambda(t) = \frac{1}{\sqrt{N_c}} \sum_{l,b} \sqrt{m_b} \exp(-i\boldsymbol{q} \cdot \boldsymbol{r}_{l,b}) \boldsymbol{e}^*_{b,\lambda} \cdot \dot{\boldsymbol{u}}_{l,b}(t) \quad , (1)$$

where N_c is the number of unit cells included in the projection, l and b index the unit cell and basis atom, respectively, m_b is the atomic mass, $\dot{\boldsymbol{u}}_{l,b}(t)$ is the atomic velocity, $\boldsymbol{r}_{l,b}$ is the unit-cell position, and $\boldsymbol{e}^*_{b,\lambda}$ is the mass-normalized polarization eigenvector. This is the normal-mode velocity projection used in the SPT reference. In the classical limit, the mode temperature is obtained from the time-averaged modal kinetic energ

$$T_\lambda = \frac{1}{k_B} \langle \dot{Q}^*_\lambda(t) \dot{Q}_\lambda(t) \rangle \quad . (2)$$

For spatial resolution, the system is divided into bins along the transport direction and the eigenmode projection is performed separately in each bin.

The heat flow is along [100], and the analyzed wave vectors lie on Γ-X with $\boldsymbol{q}$ || [100]. Modes with polarization parallel to $\boldsymbol{q}$ are assigned to the longitudinal group (LP), whereas modes with polarization perpendicular to q are assigned to the transverse group (TP). Group averaging gives the spatial temperatures $T_{LP}(x)$ and $T_{TP}(x)$, whose difference is fitted with PWCM. SPT shows stronger fixed-boundary responses for the short-wave modes, so the less boundary-sensitive long-wave modes are used

for the LP/TP coupling analysis.

The coupling between transverse and longitudinal phonons was analyzed using the PWCM, which has previously been applied to in-plane and out-of-plane phonons in monolayer graphene[34,35]. In the PWCM, two coupled heat equations are established for the transverse (t) and longitudinal (l) phonon subsystems by combining the Boltzmann transport equation with Fourier's law and introducing a coupling coefficient G_c, as follows:

$$\kappa_t \frac{d^2T_t}{dx^2} = G_c(T_t - T_l) \tag{3}$$

$$-\kappa_l \frac{d^2T_l}{dx^2} = G_c(T_t - T_l) \tag{4}$$

where T_i and $\kappa_i (i = t, l)$ are the temperature and thermal conductivity of each subsystem. Subtracting these equations yields:

$$\frac{d^2\theta}{dx^2} - \gamma^2\theta = 0 \tag{5}$$

with $\theta = T_l - T_t$, $\gamma = \sqrt{G_c(\frac{1}{\kappa_l} + \frac{1}{\kappa_t})}$. By substituting the boundary conditions $\theta|_{x\to-\infty} = 0$ and $\theta|_{x\to 0} = \theta_{max}$, the analytical solution is obtained as follows:

$$\theta(x) = \theta_{max} \exp(\gamma x) \tag{6}$$

PWCM requires two phonon groups for which effective temperatures can be defined separately and a resolvable temperature difference exists over the studied length scale. SPT yields distinct LP and TP temperature profiles along Γ-X in the free-transport region, providing the operational basis for applying PWCM. The resulting coupling length applies only to the present nanostructure, the [100] transport direction, and the selected LP/TP modes along Γ-X. It is not a Brillouin-zone average or a diamond material constant.

Following the definition used in previous graphene PWCM work, the coupling length l_c is the distance over which the LP/TP temperature difference decreases from its maximum value to 5% of that

value. The 5% threshold is an operational engineering definition, rather than a fundamental material constant fixed by the model. It is used here to apply a consistent criterion across mode groups and simulation conditions.

$$l_c = \frac{-\ln(5\%)}{\gamma} \approx \frac{3}{\gamma} = \frac{3}{\sqrt{G_c\left(\frac{1}{\kappa_l} + \frac{1}{\kappa_t}\right)}} \tag{7}$$

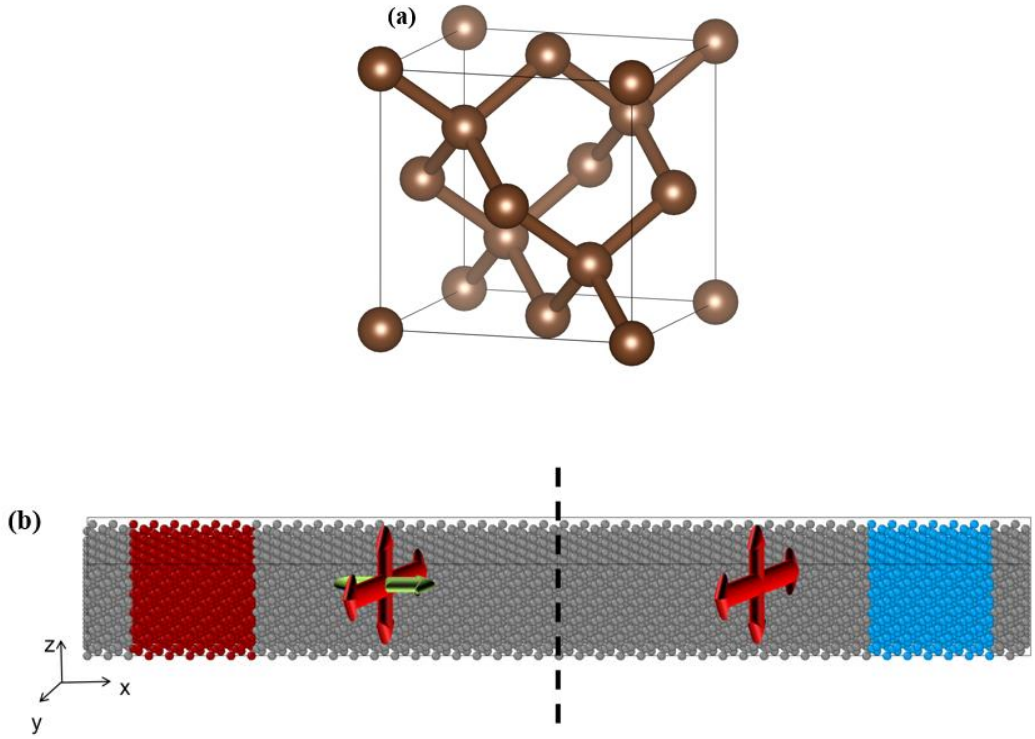

Fig. 1 (a) Schematic diagram of the diamond structure; **(b)** Schematic diagram of the simulation model for diamond.

3. Results and discussions

Figure 2(a) shows the time-averaged temperature profiles of LP and transverse TP phonons along the heat flow direction at 300 K. A distinct temperature difference between the two modes is observed, signifying local thermal nonequilibrium. This nonequilibrium arises from two factors.

On the one hand, it may originate from the selective coupling effect at the boundaries. Although uniform Langevin thermostat parameters were applied to the system in the simulation, the energy

exchange efficiency between the LP/TP modes and the thermal bath boundaries was found to be inconsistent, which is caused by the intrinsic differences in group velocity and phonon density of state. The difference in this "thermal boundary resistance" induced by the heat source allows an initial temperature difference between the two modes to be established at the boundaries.

On the other hand, a thermal resistance between modes may be caused by the finite coupling strength. In diamond, the interaction between LP and TP is relatively weak., which means that resistance exists when energy flows between the two subsystems. This finite inter-mode coupling strength hinders the rapid achievement of thermal equilibrium between LP and TP within a finite transport distance, thereby allowing the temperature difference induced by boundary effects to be maintained inside the system and form an observable distribution difference. In view of the aforementioned potential reasons, the PWCM is further introduced for quantitative analysis.

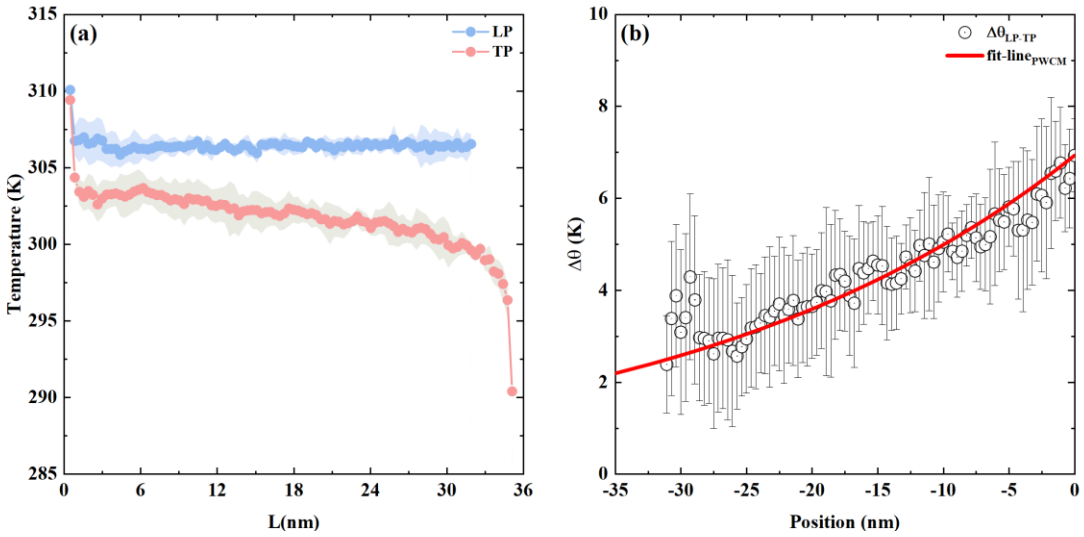

Fig. 2 (a) Spatial temperatures of longitudinal and transverse eigenmode groups along Γ-X at 300 K obtained with SPT; **(b)** $\Delta\theta = T_{LP} - T_{TP}$ and the PWCM exponential fit. The system length is approximately 35 nm. Symbols in (a) show mean temperatures and shading shows trajectory dispersion. Open circles in (b) show the mean temperature difference, error bars show trajectory dispersion, and the red line is the PWCM fit. Boundary-affected data are excluded.

For each temperature and system size, independent NEMD trajectories are generated using different initial-velocity random seeds and processed separately with SPT. LP and TP temperatures at matching spatial positions are then averaged. The mean LP/TP temperature difference is calculated and fitted with the PWCM exponential function using data from the internal free-transport region. Based on the analytical solution of the PWCM (Eq. 6), we fit the temperature difference distribution between LP and TP. In nanostructured diamond at 300 K and a system length of about 35 nm, the LP and TP branches along Γ-X retain a resolvable temperature difference in the free-transport region. PWCM fitting gives a coupling length of 130 ± 34 nm, indicating weak coupling for the selected modes. An earlier graphene study reported a coupling length of about 60 nm for the IP and OP phonon groups in a system of comparable length [35]. Because the two studies use different dimensionalities, mode groupings, and boundary conditions, this comparison concerns decay scales under the same 5% criterion and does not rank the coupling strength of diamond and graphene. The weak LP/TP coupling found here is compatible with diamond's high overall thermal conductivity: thermal conductivity combines the contributions of all phonon modes, whereas the coupling length describes the spatial relaxation of the temperature difference between selected mode groups. A high total thermal conductivity does not require all phonon groups to share one local temperature at the nanoscale.

We further examined the temperature and size dependence of l_c. As shown in Fig. 3(a), the coupling length of the selected LP/TP modes along Γ-X decreases overall with increasing temperature. Diamond has a high Debye temperature, and increasing temperature over the studied range increases the thermal population of phonon modes and anharmonic scattering. This accelerates LP/TP relaxation, so the temperature difference decays over a shorter distance. The coupling length increases overall with system length. In addition, as shown in Fig. S6, when the system temperature exceeds 700 K, the substantially enhanced anharmonic scattering causes the LP/TP temperature difference to rapidly decrease below the resolvable threshold. Consequently, the applicability condition of the PWCM is no longer satisfied, and a stable coupling length cannot be extracted. This behavior further supports the conclusion that the interbranch coupling becomes significantly stronger at elevated temperatures. In PWCM, the length

depends on both intergroup coupling and the thermal conductivities of the two groups. Thermal conductivity in a nanoscale system generally increases with length, may should increasing the distance required to reach the same fractional temperature-difference decay. As the system size increases, the number of weakly coupled phonon modes increases synchronously with the growth of the total number of phonon modes, thereby enhancing the effect of weak phonon coupling. The size dependence may therefore arise mainly from the size dependence of thermal conductivity.

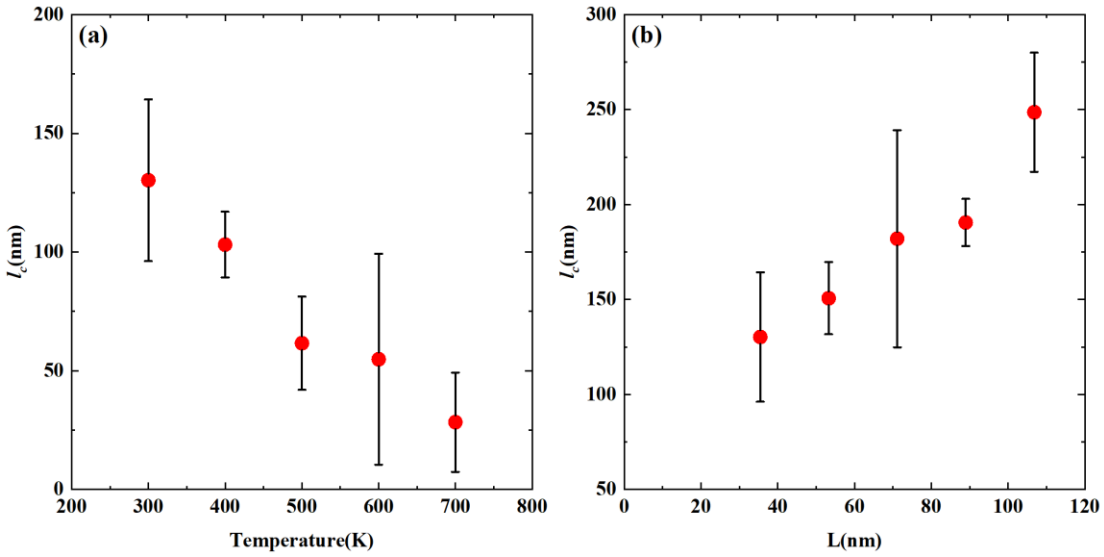

Fig. 3 (a) LP/TP coupling length as a function of temperature from 300 to 700 K; **(b)** coupling length as a function of system length L at 300 K. Symbols are obtained by fitting the mean LP/TP temperature difference. Error bars show statistical uncertainty in the PWCM coupling length and reflect fluctuations among independent simulations.

4. Conclusion

In summary, nonequilibrium molecular dynamics, the spectral phonon temperature method, and the phonon weak-coupling model were combined to quantify LP/TP coupling in nanostructured diamond. At 300 K and a system length of approximately 35 nm, the coupling length of the selected LP and TP modes along Γ-X is 130 ± 34 nm, indicating weak coupling. The coupling length decreases overall with

increasing temperature from 300 to 700 K; above 700 K, the LP/TP temperature difference falls below the resolvable threshold and a stable coupling length cannot be extracted. The coupling length increases with system length, which may mainly reflect the size dependence of thermal conductivity. Thus, local thermal nonequilibrium between distinct phonon mode groups can persist over nanoscale distances even in high-thermal-conductivity diamond.

Acknowledgment

This project is supported by the Innovation Research Foundation of National University of Defense Technology （Innovation Research Foundation of NUDT）.

Data Availability

The data that support the findings of this study are available from the corresponding author upon reasonable request.

Reference

[1] Yang H, Jia B, Xie L, Wang Z, Zhang G and Li N 2024 Joule 8 101670

[2] Han G, Cheng H, Feng Y, Chen J, Zhang Z and Zhang X 2025 Nat. Commun. 16 11059

[3] Cheng S, Guo X, Cai W, Hu Y and Tang X 2024 J. Mater. Chem. A 12 8640

[4] Martin-Gonzalez M, Lohani K and Neophytou N 2025 Energy Mater. 5 90032

[5] Li C, Luo Y, Li W, Ang R and Lee Y 2024 CHIP 3 100096

[6] Sun Y, Liu W, Guo Y, Fan Z and Chen J 2026 Int. J. Therm. Sci. 222 110597

[7] Zhang C, Rezgui H, Lian M and Zhang Z 2025 Mater. Today Phys. 59 101893

[8] Rao X, Li S, Yan Y and Cao B 2024 Microelectron. J. 145 106104

[9] Maksymowych M, Yuksel M, Hitchcock O et al 2025 Phys. Rev. Appl. 24 044019

[10] Li D, Wu Y, Kim P, Shi L and Majumdar A 2003 Appl. Phys. Lett. 83 2934

[11] Yang N, Xu X, Zhang G and Li B 2012 AIP Adv. 2 041410

[12] Tang Z, Wang X, He C and Zhou J 2024 Phys. Rev. B 110 134320

[13] Wang Y, Yan S, Wu X and Yang J 2025 Front. Phys. 20 14212

[14] Ma N, Xiao C and Xie Y 2024 Acc. Mater. Res. 5 286

[15] Dangic D 2026 Phys. Rev. B 113 024302

[16] Huang M, Liu X, Zhang P and Ren W 2021 Appl. Phys. Lett. 118 073902

[17] Bochicchio I, Sellitto A and Munafò C 2025 J. Therm. Stresses 48 1568

[18] Sidorova M, Semenov A, Zaccone A et al 2024 Phys. Rev. B 110 134513

[19] Giri A and Hopkins P 2020 Adv. Funct. Mater. 30 1903857

[20] Ferrari A 2007 Solid State Commun. 143 47

[21] Lu Z, Shi J and Ruan X 2019 J. Appl. Phys. 125 085101

[22] Lu Z, Vallabhaneni A, Cao B and Ruan X 2018 Phys. Rev. B 98 134309

[23] Pan D, Zong Z and Yang N 2022 Acta Phys. Sin. 71 20220036

[24] Xu J, Hu Y and Bao H 2023 Phys. Rev. Appl. 19 014007

[25] Guo Y, Bescond M, Zhang Z, Lannoo M, Burriel M and Volz S 2021 APL Mater. 9 091102

[26] Majumdar A and Reddy P 2004 Appl. Phys. Lett. 84 4768

[27] Sullivan S, Vallabhaneni A, Kholmanov I et al 2017 Nano Lett. 17 2049

[28] Feng T, Yao W, Wang Z, Shi J, Li C, Cao B and Ruan X 2017 Phys. Rev. B 95 195202

[29] Li D, Wang J, Jiang Y et al 2026 Mater. Adv. 7 2151

[30] Zhang K, Han X, Ershuai Y et al 2026 Appl. Phys. Lett. 128 071903

[31] Malakoutian M, Lyu J, Kasperovich A et al 2025 APL Mater. 13 041108

[32] Su Z, Han K, Ye Z et al 2025 Mater. Lett. 387 138229

[33] Wang Q, Ye Z, Liu L et al 2025 Materials 18 3882

[34] Deng C, Huang Y, An M and Cao B 2021 Mater. Today Phys. 16 100305

[35] An M, Song Q, Yu X, Cao B and Chen G 2017 Nano Lett. 17 5805

[36] Thompson A, Aktulga H, Berger R et al 2022 Comput. Phys. Commun. 271 108171

[37] Li Z, Xiong S, Sievers C et al 2019 J. Chem. Phys. 151 234105

[38] Tamaki S, Sasada M and Saito K 2017 Phys. Rev. Lett. 119 110602

[39] Tersoff J 1989 Phys. Rev. B 39 5566

[40] Tersoff J 1988 Phys. Rev. B 37 6991

Supplementary Information

Quantitatively analyzing microscopic mechanism of phonon coupling in bulk diamond

Wu Liang[1], Shixian Liu[2], Han Meng[1*], Nuo Yang[1]

[1] College of Science, National University of Defense Technology, Changsha, 410073, China.

[2] Independent Researcher, Xinzhou 034000, China.

*Corresponding authors: menghan@nudt.edu.cn (H. M.)

S1. Phonon weak coupling model

Deng[1] proposed a weak coupling model based on the extension of the Two-Temperature Model (TTM). This model primarily describes the phenomenon where phonon interactions in low-dimensional nano systems are significantly weaker than those in macroscopic systems, and it provides quantitative parameters for characterization, namely the coupling length and the coupling strength coefficient[2]. The detailed derivation process of the weak coupling model is presented below.

Defining the two subsystems and describing them using the Boltzmann transport equation:

$$\frac{\partial f_1}{\partial t} + F \cdot \nabla_p f_1 + v \cdot \nabla_r f_1 = \left(\frac{\partial f_1}{\partial t}\right)_c, \tag{S1a}$$

$$\frac{\partial f_2}{\partial t} + F \cdot \nabla_p f_2 + v \cdot \nabla_r f_2 = \left(\frac{\partial f_2}{\partial t}\right)_c, \tag{S1b}$$

where the subscripts 1 and 2 represent the two subsystems, respectively, and f denotes the phonon distribution function. The right-hand side of the equation represents the collision scattering term. When the system reaches a steady state without the application of external forces, Equations (S1a) and (S1b) can be simplified as:

$$v \cdot \nabla_r f_1 = \left(\frac{\partial f_1}{\partial t}\right)_c, \tag{S2a}$$

$$v \cdot \nabla_r f_2 = \left(\frac{\partial f_2}{\partial t}\right)_c, \tag{S2b}$$

Then, using the relaxation time approximation (RTA), Equations (S2a) and (S2b) can be written as:

$$v \cdot \nabla_r f_1 = \left(\frac{\partial f_1}{\partial t}\right)_{12} + \left(\frac{f_1 - f_{1,0}}{\tau_{11}}\right)_{ii}, \tag{S3a}$$

$$v \cdot \nabla_r f_2 = \left(\frac{\partial f_2}{\partial t}\right)_{12} + \left(\frac{f_2 - f_{2,0}}{\tau_{22}}\right)_{22}, \tag{S3b}$$

The energy exchange rate between the phonons of the two subsystems is expressed using the scattering rate, and by substituting it into Fourier's law, the transport governing equations of the system can be obtained:

$$-\kappa_1 \nabla^2 T_1 = G_c(T_2 - T_1), \tag{S5a}$$

$$-\kappa_2 \nabla^2 T_2 = G_c(T_1 - T_2), \tag{S5b}$$

where T_1 and T_2 represent the temperatures of the phonon modes in the two subsystems, respectively, κ_1 and κ_2 represent their respective thermal conductivities, and G_c is the coupling strength coefficient. Further subtracting (S5b) from (S5a) yields:

$$\frac{d^2\theta}{dx^2} - \gamma^2\theta = 0, \tag{S6}$$

where $\theta = T_l - T_t$, $\gamma = \sqrt{G_c(\frac{1}{\kappa_l} + \frac{1}{\kappa_t})}$. By substituting the boundary conditions $\theta|_{x\to-\infty} = 0$ and $\theta|_{x\to 0} = \theta_{max}$, the fitting function of the phonon weak coupling model is obtained as $\theta = \theta_{max}\exp(\gamma x)$, and the coupling length is defined as $l_c \approx \frac{\ln(5\%)}{\gamma}$.

Previous graphene weak-coupling work defined the phonon coupling length as the distance over which the temperature difference decreases to 5% of its maximum value. This operational threshold converts a continuous exponential decay into a characteristic length that can be compared consistently. If the temperature difference in the free-transport region follows

$$\theta(x) = \theta_{max}\exp(\gamma x) \tag{S7}$$

the coupling length defined using a threshold p is

$$l_c \approx \frac{-\ln(\mathrm{p})}{\gamma} \tag{S8}$$

Changing the threshold changes the absolute coupling length but not the fitted decay constant. Applying the same threshold to all simulation conditions provides a consistent basis for comparing temperature and size trends. Because diamond and graphene differ in dimensionality and mode grouping, their values represent decay scales under the same definition rather than a direct ranking of coupling strength.

If the two phonon groups have the same temperature throughout the studied region, PWCM cannot extract a coupling length from temperature-difference decay. In the approximately 35 nm system studied

here, the LP and TP modes along Γ-X retain a resolvable temperature difference and therefore satisfy the operational condition for PWCM fitting.

S2. Simulation details

<table>
<tr><td>Method</td><td colspan="6">Non-Equilibrium MD (Direct method)</td></tr>
<tr><td>Potential</td><td colspan="6">Tersoff</td></tr>
<tr><td>Function</td><td colspan="6">$$U_i = \frac{1}{2}\sum_{j\neq i} f_C(r_{ij})\,[f_R(r_{ij}) - b_{ij} f_A(r_{ij})]$$
$$f_C(r_{ij}) = f(x)$$
$$= \begin{cases} 1, & r_{ij} < R_{IJ} \\ \frac{1}{2}[1+\cos(\pi\frac{r_{ij}-R_{IJ}}{S_{IJ}-R_{IJ}})], & R_{IJ} < r_{ij} < S_{IJ} \\ 0, & r_{ij} > S_{IJ} \end{cases}$$
$$f_R(r) = A_{IJ} e^{-\lambda_{IJ} r_{ij}}$$
$$f_A(r) = B_{IJ} e^{-\mu_{IJ} r_{ij}}$$
$$b_{ij} = \chi_{IJ}(1+\beta_I^{n_I}\zeta_{ij}^{n_I})^{-\frac{1}{2n_I}}$$
$$\zeta_{ij}^{n_I} = \sum_{k\neq i,j} f_C(r_{ij}) g_{ijk}$$
$$g_{ijk} = 1 + \frac{c_I^2}{d_I^2} - \frac{c_I^2}{d_I^2 + (h_I - cos\theta_{ijk})^2}$$</td></tr>
<tr><td rowspan="4">Parameters</td><td>A_{IJ}</td><td>B_{IJ}</td><td>λ_{IJ}</td><td>μ_{IJ}</td><td>$\boldsymbol{\beta_I}$</td><td>n_I</td></tr>
<tr><td>1393.6</td><td>346.74</td><td>3.4879</td><td>2.2119</td><td>1.5724E-07</td><td>0.72751</td></tr>
<tr><td>c_I</td><td>d_I</td><td>R_{IJ}</td><td>S_{IJ}</td><td>χ_{IJ}</td><td>h_I</td></tr>
<tr><td>38049</td><td>4.3484</td><td>1.8</td><td>2.1</td><td>1</td><td>-0.57058</td></tr>
<tr><td colspan="7">Simulation process</td></tr>
<tr><td>Ensemble</td><td colspan="3">Setting</td><td colspan="3">Purpose</td></tr>
<tr><td rowspan="2">NPT</td><td>Runtime (ps)</td><td colspan="2">100 ps</td><td colspan="3" rowspan="2">Relax structure</td></tr>
<tr><td>Temperature (K)</td><td colspan="2">300 K</td></tr>
</table>

	Boundary condition	X, Y, Z: f, p, p		
NVE	Runtime (ps)	400ps		Prerun & Relax system
	Boundary condition	X, Y, Z: f, p, p		
	Thermostat	Heat source	310 K	
		Heat sink	290 K	
NVE	Runtime (ns)	5 ns		Record information
	Boundary condition	X, Y, Z: f, p, p		
	Thermostat	Heat source	310 K	
		Heat sink	290 K	
Recorded physical quantity				
Temperature		$\langle E \rangle = \sum_{i=1}^{N} \frac{1}{2} m v_i^2 = \frac{1}{2} N k_B T_{MD}$		
Heat flux		$J = \frac{1}{N_t} \sum_{i=1}^{N_t} \frac{\Delta \varepsilon_i}{2 \Delta t}$		
Thermal conductance		$\kappa = -\frac{J}{A \cdot \Delta T}$		

S3. Spectral phonon temperature method

The conventional molecular-dynamics temperature is calculated from the kinetic energy of all atoms and does not distinguish phonon eigenmodes with different wave vectors and polarizations. Spectral phonon temperature method (SPT) [3] obtains mode-resolved temperatures by projecting NEMD velocity trajectories onto lattice-dynamical eigenmodes and defining temperature from the mean projected kinetic energy. For a mode specified by $\boldsymbol{q}$ and λ, the atomic displacement can be expanded as

$$\boldsymbol{u}_{l,b}(t) = \frac{1}{\sqrt{N_c m_b}} \sum_{q,\lambda} Q_\lambda(\mathrm{t}) \boldsymbol{e}_{b,\lambda} \exp(i\boldsymbol{q} \cdot \boldsymbol{r}_{l,b}) \tag{S9}$$

where N_c is the number of unit cells, l and b index the unit cell and basis atom, m_b is the atomic mass, $\boldsymbol{r}_{l,b}$ is the equilibrium unit-cell position, $\boldsymbol{e}_{b,\lambda}$ is the mass-normalized polarization eigenvector, and $Q_\lambda(\mathrm{t})$ is the normal-mode coordinate. Differentiation with respect to time gives the atomic velocity

$$\dot{\boldsymbol{u}}_{l,b}(t) = \frac{1}{\sqrt{N_c m_b}} \sum_{q,\lambda} \dot{Q}_\lambda(t) \boldsymbol{e}_{b,\lambda} \exp(i\boldsymbol{q} \cdot \boldsymbol{r}_{l,b}) \tag{S10}$$

Using the orthonormality of the polarization eigenvectors, the mass-weighted normal-mode velocity is obtained from the atomic velocities:

$$\dot{Q}_\lambda(t) = \frac{1}{\sqrt{N_c}} \sum_{l,b} \sqrt{m_b} \exp(-i\boldsymbol{k} \cdot \boldsymbol{r}_{l,b}) \boldsymbol{e}^*_{b,\lambda} \cdot \dot{\boldsymbol{u}}_{l,b}(t) \tag{S11}$$

Equation (S11) is the central SPT projection relation and corresponds to the normal-mode velocity projection in the SPT reference. It decomposes real-space velocities into modes with specified wave vectors and polarization eigenvectors. The center-of-mass velocity is removed before projection to avoid contamination of low-frequency modes. The instantaneous kinetic energy of mode(q, λ) is

$$E_{K,\lambda}(t) = \frac{1}{2} \dot{Q}^*_\lambda(t) \dot{Q}_\lambda(t) \tag{S12}$$

In the classical limit, equipartition gives the mode temperature as

$$T_\lambda = \frac{1}{k_B} \langle \dot{Q}^*_\lambda(t) \dot{Q}_\lambda(t) \rangle \tag{S13}$$

S4. Selective constraint boundary and fitting region

The branch-selective velocity constraint establishes a nonequilibrium state between the LP and TP modes near one boundary. It follows the approach used in electron–phonon two-temperature models and previous PWCM studies, where a selective boundary generates a temperature difference between two energy subsystems and its spatial relaxation is used to characterize coupling. The constraint is not used to define the LP/TP eigenbranches. Because it changes the equations of motion locally, the constrained region and its neighboring bins are excluded from temperature extraction and coupling-length fitting.

Fixed layers, thermal baths, and bins adjacent to both interfaces are also excluded. Along Γ-X, $\boldsymbol{q}$, the heat-flow direction, and x are all parallel to [100]. LP and TP modes are classified from the orientation of their polarization eigenvectors relative to $\boldsymbol{q}$ and their temperatures are obtained with SPT. The reported coupling length is therefore fitted from the eigenvector-resolved LP/TP temperature difference in the internal free-transport region, rather than from locally perturbed states near the constrained interface.

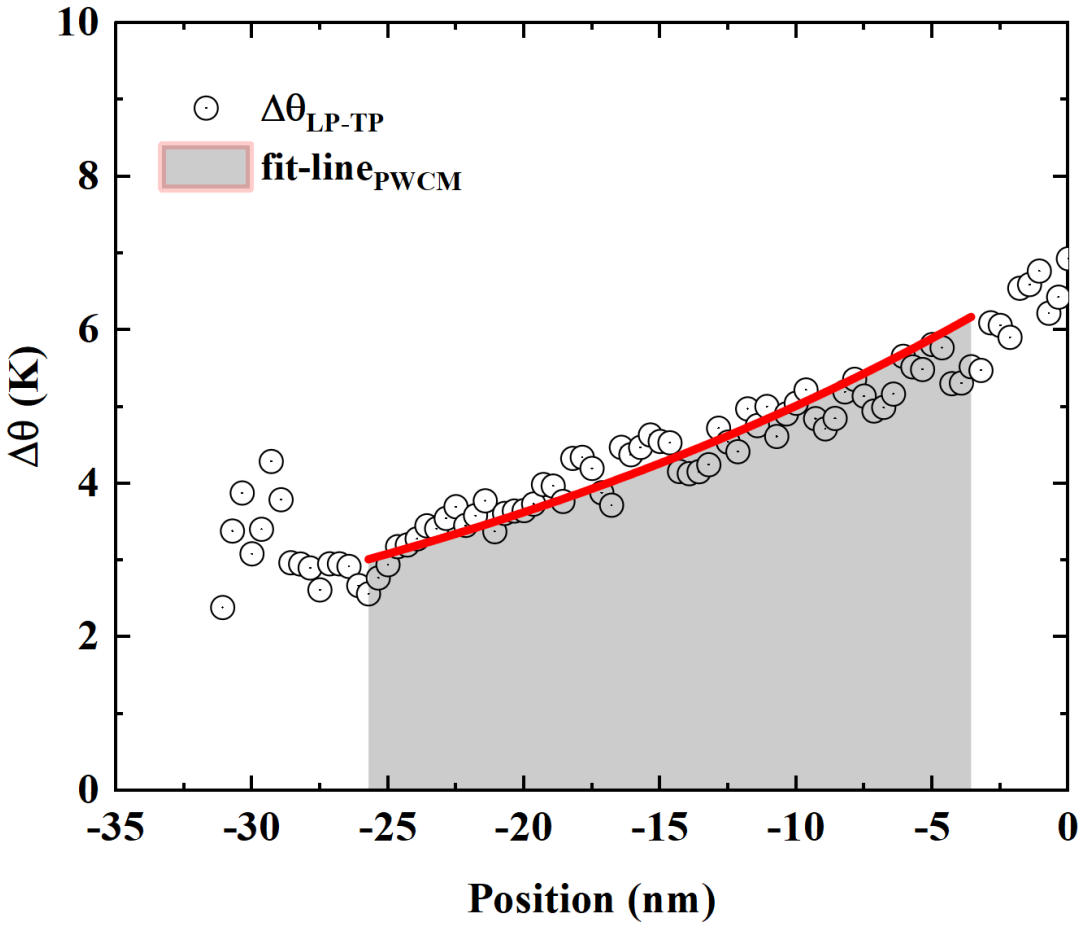

Fig. S4. LP/TP eigenmode temperature difference along Γ-X obtained with SPT and its PWCM fit. Open circles show the branch temperature difference and the red line shows the exponential PWCM fit. The light-blue region between the two vertical blue lines is the fitting interval. Data near the thermal-bath and selective-constraint interfaces are excluded. The red curve outside the fitting interval is only an extrapolation of the fitted function.

S5. Boundary response and mode selection at different wavelengths

To assess finite-size and fixed-boundary effects on mode temperatures, the Γ-X path along [100] is described using the normalized wave vector $\boldsymbol{q}/\boldsymbol{q}_{max}$, where $\boldsymbol{q}_{max}$ is the magnitude at X. Because wavelength is inversely proportional to wave-vector magnitude, modes near Γ have relatively long wavelengths and modes near X have relatively short wavelengths. The sampled Γ-X points are divided approximately into low-, intermediate-, and high-wave-vector ranges for comparison. Figure S5(a,b) shows that modes in the first two ranges are more sensitive to the fixed boundaries. Several branches exhibit weak spatial gradients or depart from a diffusive temperature profile, indicating characteristic transport lengths comparable to or greater than the approximately 35 nm system length and hence quasiballistic behavior. A PWCM fit to these modes would contain substantial finite-size and boundary contributions.

In contrast, the high-wave-vector modes in Fig. S5(c) exhibit clearer and more continuous temperature variations in the internal free-transport region and are less affected by the fixed boundaries. Their LP/TP temperatures are therefore used for the subsequent temperature-difference analysis and PWCM fitting, reducing the influence of quasiballistic transport in the lower-wave-vector modes.

The high-wave-vector modes remain locally perturbed near the fixed boundaries, thermal baths, and selective-constraint interface. These regions and neighboring bins are excluded from the fit. The coupling length is extracted only from the LP/TP temperature difference in the internal free-transport region.

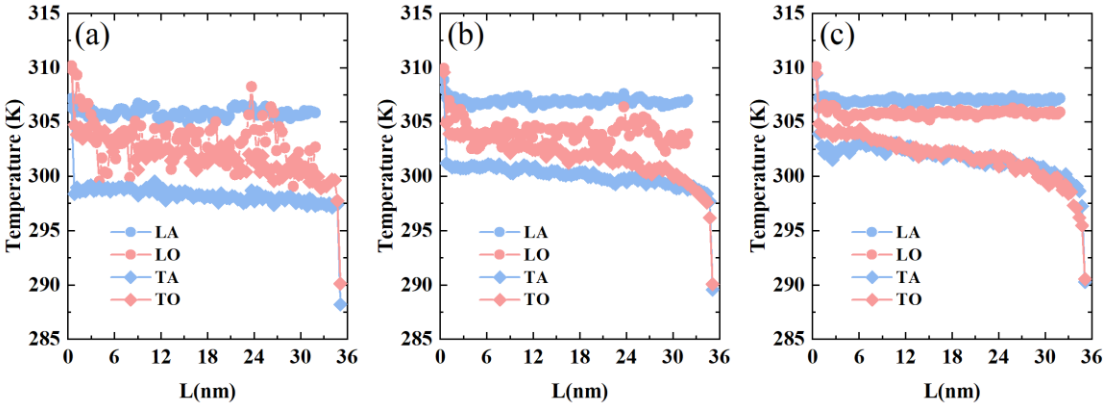

Fig. S5. Branch-resolved SPT temperature profiles for (a) long-, (b) intermediate-, and (c) short-wave modes along Γ-X. Circles and diamonds denote longitudinal and transverse branches; LA, TA, LO, and TO denote longitudinal acoustic, transverse acoustic, longitudinal optical, and transverse optical branches.

S6. Spatial temperature profiles of the LP/TP mode groups at different temperatures.

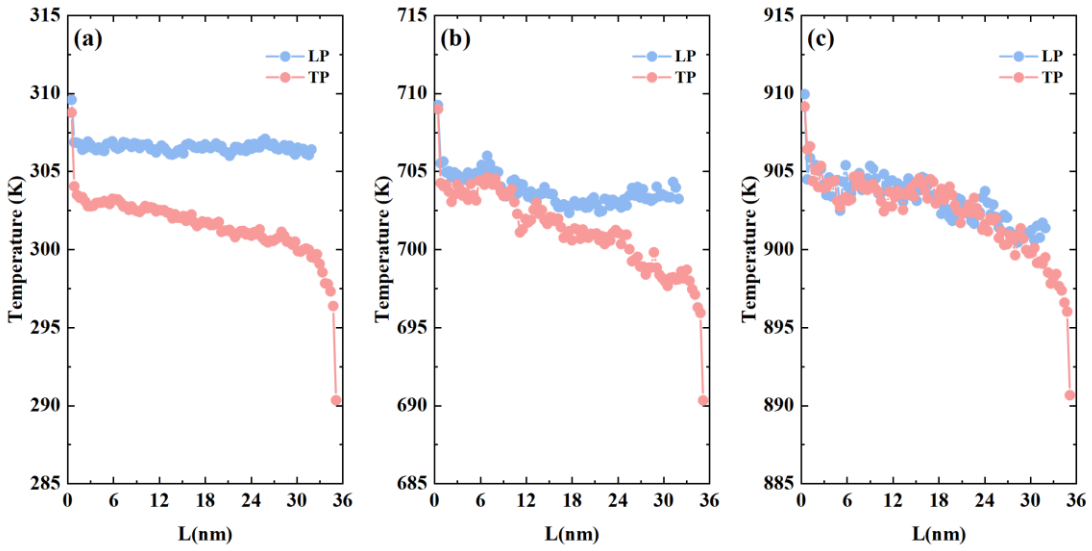

Fig. S6. Spatial temperature profiles of the selected short-wave LP/TP mode groups along Γ-X at average temperatures of (a) 300 K, (b) 700 K, and (c) 900 K. Blue and red symbols denote the LP and TP branches, respectively. The LP/TP temperature difference decreases as the system temperature increases; above 700 K the two temperatures nearly overlap and PWCM is no longer applicable.

Reference

1. S. Sullivan, A. Vallabhaneni, I. Kholmanov, et al., “Optical Generation and Detection of Local Nonequilibrium Phonons in Suspended Graphene,” *Nano Lett*. 17(3), 2049-2056 (2017).

2. M. An, Q. Song, X. Yu, B. Cao, and G. Chen, “Generalized Two-Temperature Model for Coupled Phonons in Nanosized Graphene,” Nano Lett. 17(9), 5805-5810 (2017).

3. T. Feng, W. Yao, Z. Wang, J. Shi, C. Li, B. Cao, and X. Ruan, “Spectral analysis of nonequilibrium molecular dynamics: Spectral phonon temperature and local nonequilibrium in thin films and across interfaces,” Phys. Rev. B 95(19), 195202 (2017).